Article

Influence of Precipitation on the Mechanical Properties and Age-hardening Response of Mg–10Sn

Sustainable Manufacturing and Foundry Practices
1(1) 52–63, 2026

DOI: 10.1177/IIF.261437165
Journal.indianfoundry.org
THE INSTITUTE OF INDIAN FOUNDRYMEN

Tapabrata Maity[1], Sonika Chahar[1], Palash Poddar[2], Konda Gokuldoss Prashanth[3] and Debdas Roy[1]

Abstract

Comprehensive attention has been focused globally on producing lightweight Mg-based alloys for automotive applications, which can perform well at operating temperatures (200–300°C). This study examines the age-hardening behavior of Mg–10Sn alloys for enhanced performance. Room-temperature tensile investigations show that artificially aging for 100 h at 200°C maximizes both tensile strength and ductility. Thermal aging at 200°C for 100 h significantly increases work hardening capabilities, evidenced by a high strain-hardening rate ($\theta = 2.10$) and a hardening exponent (n) of 0.4167. This elevates the necking stress to 122 MPa and boosts load-bearing capacity (H_C) from H_C = 0.63 to 0.75 in Mg–10Sn alloy. The observed trend in strain-hardening behavior suggests a two-stage work-hardening response, driven by the precipitation of Mg_2Sn intermetallic at α-Mg grain boundaries, which significantly enhances the strength.

Keywords

Mg–10Sn alloy, age hardening, mechanical properties, tensile behavior

[1]Materials and Metallurgical Engineering Department, National Institute of Advanced Manufacturing Technology (formerly NIFFT), Hatia, Ranchi, Jharkhand, India
[2]National Metallurgical Laboratory, Jamshedpur, Jharkhand, India
[3]Department of Mechanical and Industrial Engineering, Tallinn University of Technology, Tallinn, Estonia

Corresponding author:
Debdas Roy, Materials and Metallurgical Engineering Department, National Institute of Advanced Manufacturing Technology (Formerly NIFFT), Hatia, Ranchi 834003, Jharkhand, India.
E-mail: droy2k6@gmail.com

Introduction

Magnesium alloys provide a good balance of exceptional damping capacity, superior heat dissipation, high specific strength, superior castability, and machinability for lightweight structural materials (Ghosh & Naryanan, 2008). Recently, in the automobile and aerospace sectors, the demand for lightweight material has inevitably increased to reduce gas emissions and save fuel consumption. Promisingly, Mg-alloys, particularly die-cast Mg–Zn and Mg–Al, offer superior strength-to-weight ratios than aluminum (Pollock, 2010; Wang, M. Y. et al., 2012). Further, with the need for weight reduction, Mg-alloys are increasingly used in the automobile sector for components like steering columns, steering wheels, gearboxes and seat frames (Kimura et al., 2009).

Medium-strength Mg–Sn and Mg–Sn–Al alloys are prime auto body-sheets candidates, offering superior formability, high specific strength, and resistance to corrosion (Nakata & Kamado, 2023; Wan et al., 2021). While at low temperatures, Mg-alloys show poor formability due to their hexagonal crystal structure (hcp), fewer slip systems, and a pronounced basal texture (Elsayed et al., 2013). Alloying tunes the structural properties, but high concentrations limit room-temperature ductility (Peng et al., 2023).

AZ91 and AM Mg-alloys are preferred for automobile structural components due to superior castability and strength (Koren et al., 2002; You et al., 2017). However, high-temperature instability limits their use in high-temperature applications; likewise, the low melting point (437°C) of the Mg17Al12 phase compromises creep resistance (Srinivasan et al., 2010). Mg–Sn system remains a promising heat-resistant alloy under thermal load (Gibson et al., 2010). High tin (Sn) solubility (~14.7%) facilitates significant precipitation hardening via Mg_2Sn precipitation, and its high melting point (770°C) provides superior thermal stability than Mg-RE systems. However, Sn imposes poor ductility. Brittle Mg_2Sn phases along the grain boundaries deteriorate ductility, limiting their usage in automotive sectors (Mendis et al., 2006). Moreover, as tin is a non-toxic and necessary element, the Mg–Sn system holds enormous promise in biomedical implants.

Enhancing age-hardening ability is popular in metallic materials to improve mechanical performance in metallic alloys. Artificial aging is traditionally used to tailor the age-hardening behavior of various Mg-alloys, which include Mg–Sn (Mendis et al., 2006), Al-Mg–Zn (Deng et al., 2023), Mg-RE (Li et al., 2019), Mg-Si (Yamamoto et al., 2020), and Al–Mg–Si (Zhu et al., 2019). This study investigates the age-hardening response of Mg–10Sn alloys at operating temperatures of 200-300ºC and its impact on mechanical properties. This temperature range is relevant, as it matches the standard warm forming condition often employed for Mg-based sheets.

Experimental

An Mg–10Sn (wt%) alloy was fabricated via casting. Initially, a portion of the total Mg was charged and melted in a crucible inside a furnace, and then adequate Sn was added. To avoid excessive oxidation during melting, the stepwise-charging practice of Mg ingots was adopted. The oxide layer on the top was skimmed out completely

and regularly. Following flux application and addition of Sn, the mixture was held for 30 min at 750°C to ensure complete dissolution. Subsequently, the melt was cast into ingots in a preheated crucible (250°C) inside a furnace in an argon atmosphere. Then cast samples were subjected to T4 treatment, which involved heating to 300°C for 8 h. followed by water quenching to room temperature. The process (T4) was conducted in a mild steel box covered with sand to avoid oxidation. Finally, the samples were artificial aged (T6) in a muffle furnace in an oil bath at 200°C for 100 and 500 h, respectively. At regular intervals, samples were removed from the furnace and quenched in water at room temperature. The resulting conditions were denoted as 100 h/200°C and 500 h/200°C Mg–10Sn alloys, respectively.

Tensile property was evaluated using specimens with dimensions of 30 × 6 × 6 mm^3 using Instron 8501 universal testing machine at a crosshead velocity and strain rates of 0.03 mm/s and 10^{-3}/s, respectively. Tensile samples were prepared using wire electrical discharge machining. To mitigate data fluctuations caused by shrinkage porosity, all samples were extracted from the center of the ingots. Structure and microstructure of the cast and aged specimens were identified using a Rigaku SmartLab, Japan X-ray diffractometer (40 kV/40 mA) with Cu–Kα radiation and JEOL-JSM840A scanning electron microscope (SEM) fitted with an energy-dispersive spectroscope (Oxford Instruments, Abingdon, UK). The microstructure after tensile deformation was investigated by SEM. Vickers hardness was measured using a Leica-VMHT, Germany, tester with 25 gf load and 10 s dwell time.

Results and Discussion

Phase Structure Identification

Figure 1 shows the XRD spectrum of the as-cast and 100 h/200°C and 500 h/200°C Mg–10Sn specimens. It reveals peaks from *hcp* α-Mg as the primary solid solution and intermetallic β-Mg_2Sn phases only. The calculated average crystallite size (D) and lattice parameter (α) of the phases are shown in Table 1. It shows prolonged aging increases the crystallite size in both α-Mg and β-Mg_2Sn precipitates significantly, while their lattice parameters remain unaltered. Furthermore, mass fraction calculations indicate the occurrence of precipitation reaction in the sample aged at 200°C for 100 h, which shows reaching a peak volume of β-Mg_2Sn precipitates up to $V_f^{\beta}{}_{100}$ = 19%. While aging continues to 500 h, the mass fraction of these precipitates declined to $V_f^{\beta}{}_{500}$ = 11%.

Effect of Aging on the Microstructural Formation

Figure 2 displays the optical micrograph of the alloy in as-cast, 100 h/200°C, and 500 h/200°C conditions. The microstructure of the cast alloy shows a dendritic morphology, characterized by a brighter matrix and a darker eutectic phase localized in the interdendritic regions. However, samples aged at 200°C for 200 and 500 h exhibited significant coarsening of dendrites, which increased with holding time. High-resolution SEM images in Figure 3(a–c) show a microstructure composed of a bright, primary α-Mg matrix and a dark, semi-coherent network of

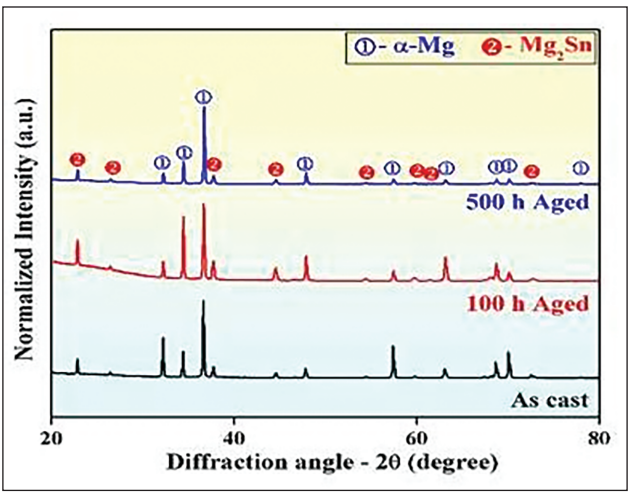

Figure 1. X-ray Diffraction Analysis of the As-cast, 100 h/200°C, and 500 h/200°C Samples Revealed a Phase Composition Consisting of Primary hcp α-Mg Solid Solution and Intermetallic β-Mg_2Sn.

Table 1. X-ray Diffraction Profile Analysis Data Showing the Lattice Parameter and Crystallite Size for the As-cast, 100 h/200°C, and 500 h/200°C Mg–10Sn specimens.

Sample Description	Lattice Parameter – α (Å)		Crystallite Size – *D* (Å)	
	α-Mg	β-Mg_2Sn	α-Mg	β-Mg_2Sn
As-cast	3.212 ± 0.002	6.754 ± 0.004	278 ± 24	384 ± 16
100 h/200°C	3.210 ± 0.002	6.756 ± 0.001	647 ± 62	556 ± 12
500 h/200°C	3.200 ± 0.002	6.761 ± 0.003	1,224 ± 49	1,019 ± 41

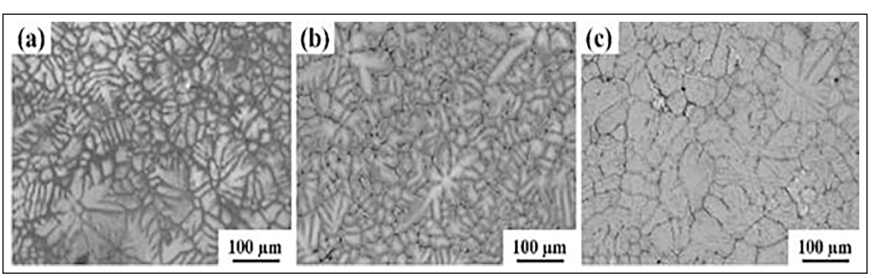

Figure 2. The Optical Micrography Images Show the Microstructure of the Mg10Sn Alloys in the Following Conditions: (a) as-cast, (b) 100 h/200°C, and (c) 500 h/200°C, respectively.

α-Mg+β-Mg_2Sn eutectic mixture located along the grain boundaries (Zhang et al., 2017). Additionally, traces of lath-shaped β-Mg_2Sn precipitates are present within the α-Mg grains. Figures 3b and c show that the amount of lath-shaped β-Mg_2Sn precipitates increases with aging time (Table 2). Hence, as high-temperature (300°C) T4 treatment facilitates Sn diffusion into the matrix to form a solid

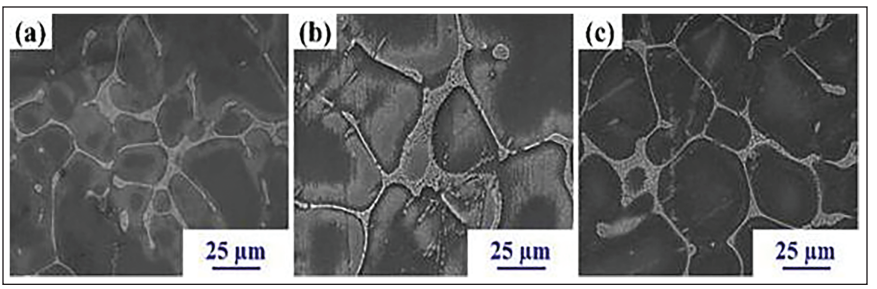

Figure 3. SEM Images Revealing the Microstructure of (a) as-cast specimen consists of primarily the α–Mg matrix (dark areas), and Sn-rich eutectic (α-Mg+β-Mg_2Sn) segregated along the Mg grain boundaries forming a semicontinuous network. However, traces of β-Mg_2Sn can be found within the matrix of α-Mg grains in a lath-shaped structure in the thermally treated (b) 100 h/200°C and (c) 500 h/200°C Mg–10Sn specimens.

Table 2. X-ray Diffraction Profile Analysis Data Furnishing the Volume Fraction of α-Mg and β-Mg_2Sn Phases Present in the As-cast, 100 h/200°C, and 500 h/200°C Mg–10Sn Specimens.

	Lattice Parameter – α (Å)	
Sample Description	α-Mg (V_f^{α})	β-Mg_2Sn (V_f^{β})
As-cast	91 ± 4	9 ± 4
100 h/200°C	81 ± 1	19 ± 1
500 h/200°C	89 ± 1	11 ± 1

solution, quenching suppresses Sn diffusion, resulting in a lath-shaped β-Mg_2Sn precipitate. Conversely, holding at a lower temperature (200°C) for 100 and 500 h (in aged 100 h/200°C and 500 h/200°C specimens) causes slow Sn diffusion, leading to an increased concentration/formation of the eutectic structure ($V_f{}^{\beta}{}_{100}$ = 19% and $V_f{}^{\beta}{}_{500}$ = 11%). Further aging up to 500 h, Sn partitions into the eutectic α-Mg+β-Mg_2Sn, leading to a continuous network morphology accompanied by the coarsening of the eutectic phases.

Influence of Precipitation on the Mechanical Property

The room-temperature engineering tensile stress–strain curves are shown in Figure 4a and are documented in Table 3. The as-cast specimen showed a yield strength of $\sigma_y \sim 76$ MPa, a tensile strength $\sigma_U \sim 137$ MPa, and a fracture strain of $\varepsilon_f \sim 4\%$. While aging at 200°C left σ_y nearly unchanged ($\sigma_y \sim 75$ MPa) for 100 h before it declines to $\sigma_y \sim 68$ MPa after 500 h. Nevertheless, σ_U peaks at approximately $\sigma_U \sim 145$ MPa after 100 h of aging before it subsequently declines to $\sigma_U \sim 126$ MPa after 500 h aging. Prolonged aging reduced ductility from $\varepsilon_f \sim$ 4.25% (100 h) to $\varepsilon_f \sim 3$ % (500 h). Furthermore, the 500 h/200°C specimen exhibited more pronounced serrations in tensile curves, suggesting unstable plastic flow.

Fracture Analysis

Figure 4 (b–d) shows fracture surface morphology of the as-cast, 100h/200°C, and 500h/200°C specimens, respectively. In the cast specimen (Figure 4b), the region around marked *A* shows smooth brittle facets, *B* shows small dimples (plastically deformed area), *C* shows cavities formed by the extraction of grains, *D* shows flutes, and *F* shows small dimples. Flutes are striations or river patterns which are a common fractographic feature in *hcp* materials (Merson et al., 2020). Fluted fracture surfaces typically result from nucleation of tubular voids at the intersection of basal slip and prismatic/pyramidal slip bands. Flat facets and flute patterns indicate a cleavage mode of fracture in the as-cast specimens, while localized small dimples suggest the prior plastic deformation before failure, leading to quasi-cleavage fracture in the cast Mg–10Sn alloy (Jiang et al., 2023; Merson et al., 2020). While the fracture surface of the 100 h/200°C specimen in Figure 4(c) shows the presence of quasi-cleavage, the presence of deeper dimples suggests extensive plastic deformation (Kondori etal., 2014; Shabani et al., 2019). Fracture surface of the 500 h/200°C specimen (Figure 4d) shows flutes or a river pattern, marking the evidence of PLC event recorded during tensile deformation. Further, fluted surfaces around *A–B* show a small amount of plastic deformation around *C*, indicating a quasi-cleavage mode of fracture. Additionally, cracks around the GBs show specimens' poor ductility and brittleness.

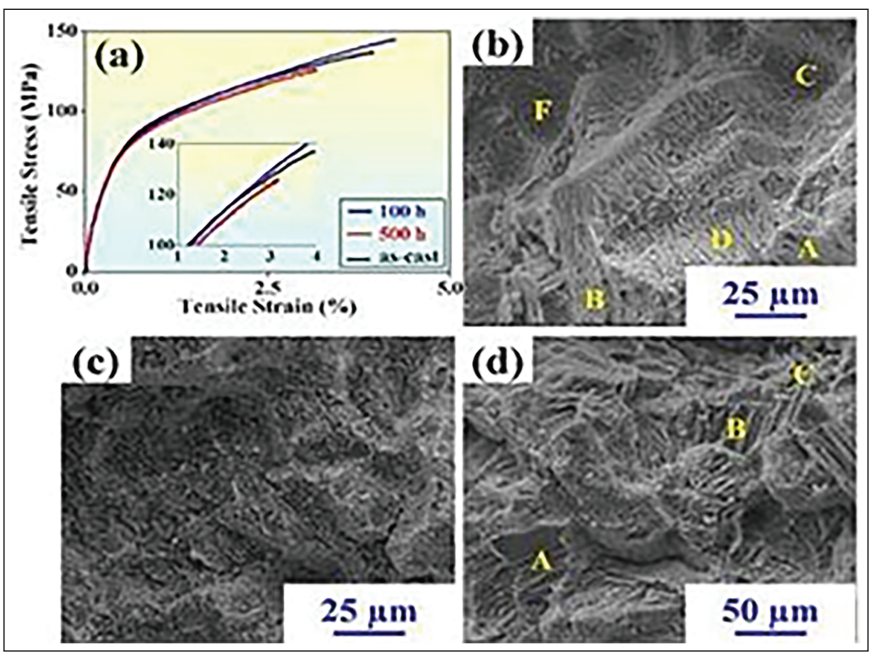

Figure 4. (a) Tensile engineering stress–strain curves for the as-cast, 100 h/200°C, and 500 h/200°C specimens at room temperature. (b)–(d) show their corresponding fracture surface morphology of the cast, 100 h/200°C, and 500 h/200°C alloys, respectively.

Age-hardening Response as a Function of Aging Time

Table 3 shows Young's modulus (E) of the specimens gradually increasing with the aging duration from up to 24 GPa, while hardness values remain unaltered. Figure 5 shows the effect of AA on hardness and mechanical properties as a function of aging duration.

Work-hardening Capacity (σc)

The work-hardening capacity ($\sigma_C = \sigma_S / \sigma_y - 1$) was assessed to evaluate the deformation behavior of the cast and aged specimens. As shown in Table 3, the aged alloys exhibited superior load-bearing ability with σ_C values reaching $\sigma_C \sim 0.75$ compared to $\sigma_C \sim 0.63$ for the as-cast state (Afrin et al., 2007; Luo et al., 2006). Thus, β-Mg_2Sn precipitate phases are vital to the load-bearing ability of the Mg–10Sn alloy.

Strain-hardening Rate (θ)

Figure 6 shows the representative strain-hardening rate ($\theta = d\sigma_T / d\varepsilon_T$, where σ_T and ε_T are true stress and true strain, respectively) vs. true strain curves (Shi et al., 2023). Throughout the plastic deformation regime, the 100 h/200°C specimen shows a higher strain-hardening rate ($\theta = 2.10$) than both the as-cast

Table 3. The Room-Temperature Mechanical Properties Data Observed for the Mg–10Sn As-cast, 100 h/200°C and 500 h/200°C Aged Samples, Respectively.

Alloy Designation	σ_Y (MPa)	σ_{UTS} (MPa)	ε_f (%)	Hardness (HV)	E (GPa)	σ_c	θ
As-cast	76.0	137.0	4.0	41.0	19.0	0.63	2.02
100 h/200°C	75.0	145.0	4.3	41.2	20.0	0.75	2.10
500 h/200°C	68.0	126.0	3.0	41.7	24.0	0.75	1.73

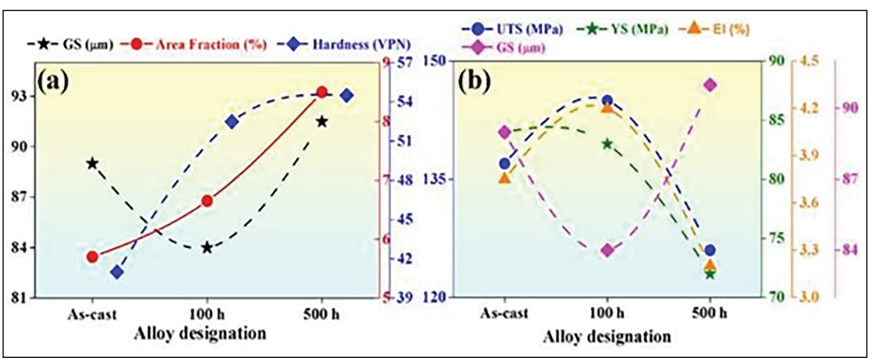

Figure 5. The Plot Shows the Hardness and Mechanical Properties of the Mg–10Sn alloy in the As-cast, 100 h/200°C, and 500/200°C Alloys as a Function of Aging Duration.

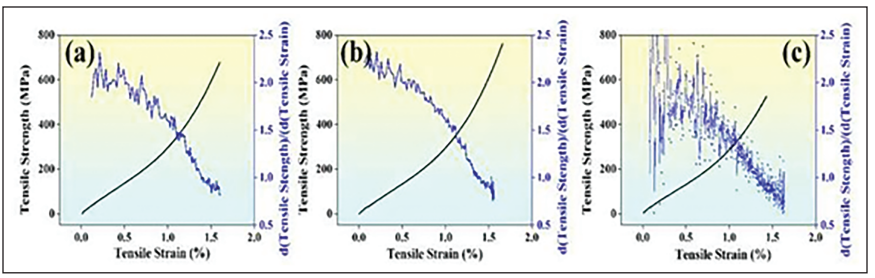

Figure 6. Representative Strain-Hardening Rate – True Strain Curves from the Engineering Tensile Data of the As-cast, 100 h/200°C, and 500 h/200°C Specimens, Respectively.

(θ = 2.02) and 500 h/200°C (θ = 1.73) samples. Further, the onset of necking (plastic instability) occurred at the highest strain (ε_T = 0.45) in the 100 h/200°C specimen (σ_T = 122 MPa), reflecting superior ductility compared to 500 h/200°C (ε_T = 0.39, σ_T = 58 MPa) and as-cast specimen (ε_T = 0.38, σ_T = 103 MPa). Apart from that, the gradual decline of θ up to plastic instability (Figure 6) suggests that age-hardened Mg–10Sn alloys undergo steady-state work hardening.

Strain-hardening Exponent (n)

Hollomon expressions were utilized to determine the strain-hardening exponent (n) (Shabani et al., 2019):

$$\sigma = K\varepsilon^n, \tag{1}$$

$$n = d\left(ln\sigma\right) / d\left(ln\varepsilon\right), \tag{2}$$

where σ, ε, and K correspond to stress, strain, and constant, respectively, listed in Table 4. Figure 7 shows that the 100 h/200°C specimen exhibited the maximum strain-hardening exponent (n = 0.4167), which signifies superior formability compared to the as-cast (n = 0.4065) and the 500 h/200°C (n = 0.3947) specimens. Further, the dual-slope behavior suggests a transition from a high-rate non-homogeneous deformation (n_1) to a lower/moderate homogeneous deformation (n_2) regime. These values match high-formability standards (0.2–0.5) and are comparable to Mg–Yb (n = 0.45) (Zhang et al., 2021) and Mg–3Al–3Sn (n = 0.45) (Wang, H. Y. et al., 2012) and surpass several high-strength steels (Chen et al., 2005; Xu et al., 2012).

Discussion

In the initial regime, the 100 h/200°C specimen (where n_1 = 0.6232) relies on precipitate to bear the primary load during deformation. Interestingly, the 500 h/200°C specimen reached a maximum n_1 = 0.6433, which correlates with its

Table 4. The Strain Hardening Exponents (n) Calculated from the Room-temperature Mechanical Test Observed for the Mg–10Sn As-cast, 100 h/200°C and 500 h/200°C Samples, Respectively.

Alloy Designation	η	R^2	η_1	R^2	η_2	R^2
As-cast	0.4065	0.9321	0.6191	0.9832	0.2660	0.9994
100 h/200°C	0.4167	0.9497	0.6232	0.9864	0.3039	0.9984
500 h/200°C	0.3947	0.9549	0.6433	0.9921	0.2999	0.9938

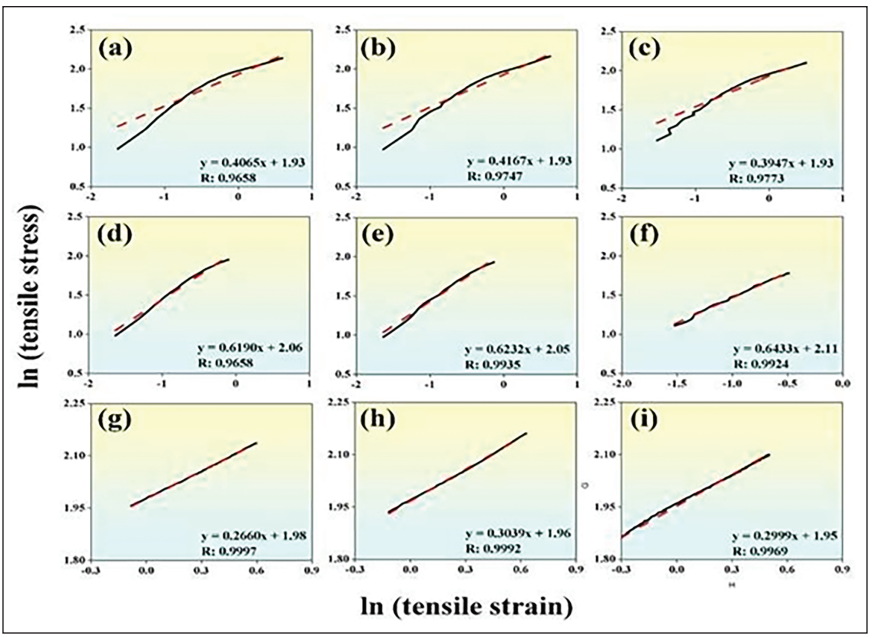

Figure 7. Data Postulating the Constructive Parameters of the Hollomon Expression Revealing the Two Regimes During Strain Hardening Where the 100 h/200°C Alloy Has the Highest Strength with True SHE 0.3039 Than the As-cast and 500 h/200°C Sample.

elevated Young's modulus of 24 GPa. During the second regime ($n_2 = 0.3039$), the 100 h/200°C specimen transitions to more homogeneous deformation facilitated by the particle–matrix interactions. The 100 h/200°C specimen achieves a superior average SHE, $n = 0.4167$, because its microstructure contains a maximum volume fraction of β-Mg_2Sn (19%) precipitates. During the second hardening stage ($n_2 = 0.3039$), this microstructure delays localized deformation, effectively extending uniform strain and enhancing ductility. These observations are consistent with fractographic evidence showing superior plastic flow in the 100 h/200°C specimens.

Mechanistically, the high-volume fraction of β-Mg_2Sn ($V_f^{\beta} = 19\%$) phase precipitates act as the primary load-bearing phase within the α-Mg matrix. In Mg–10Sn alloy, it is evident that precipitation on α-Mg grain matrix significantly

enhances the age-hardening response compared to basal precipitation (Nie, 2003). In the 100 h/200°C specimen, these precipitations are more prevalent than in the 500 h/200°C specimens. Consequently, as strain increases, dislocation–dislocation interactions on the slip planes are intensified by the precipitation's barriers. The limited ability of dislocations to bypass these particles results in a high hardening rate (θ = 2.10), ultimately yielding a superior combination of ductility ε_f = 4.3%, strength σ_S = 145 MPa, and load-bearing capacity, σ_C = 0.75.

Conclusions

Based on the findings, we conclude:

1. 1. Artificial aging (AA) at 200°C for 100 h effectively facilitates the precipitation of β-Mg_2Sn strengthening phases with a peak volume fraction of 19%. In contrast, exceeding the aging duration to 500 h results in over-aging, characterized by coarser β-Mg_2Sn precipitates and a coarser eutectic structure compared to the 100 h condition.
2. 2. The specimens aged at 200°C for 100 h achieve an optimal balance of mechanical properties and superior strain-hardening rate (θ = 2.10). This performance is significantly attributed to β-Mg_2Sn reinforcement (V_f = 19%), which functions as the primary load-bearing constituent.
3. 3. Fractographic analysis confirms a transition toward a more ductile quasi-cleavage mode in the 100-h aged specimen, supported by the deeper dimples, stable plastic flow and superior formability (n = 0.4167).

Declaration of Conflicting Interests

The authors declared no potential conflicts of interest with respect to the research, authorship, and/or publication of this article.

Funding

The authors received no financial support for the research, authorship, and/or publication of this article.

References

Afrin, N., Chen, D. L., Cao, X., & Jahazi, M. (2007). Strain hardening behavior of a friction stir welded magnesium alloy. *Scripta Materialia*, *57*(11), 1004–1007.

Chen, X. H., Lu, J., Lu, L., & Lu, K. (2005). Tensile properties of a nanocrystalline 316L austenitic stainless steel. *Scripta Materialia*, *52*(10), 1039–1044.

Deng, Y., Sun, W., Yang, Y., Zhan, H., Yan, K., & Zeng, G. (2023). Effects of Mg2Sn precipitation on the age-hardening and deformation behaviour of a Mg–Sn–Al–Zn alloy. *Materials Science and Engineering: A*, *867*, 144714.

Elsayed, F. R., Sasaki, T. T., Mendis, C. L., Ohkubo, T., & Hono, K. (2013). Compositional optimization of Mg–Sn–Al alloys for higher age hardening response. *Materials Science and Engineering: A*, *566*, 22–29.

Gibson, M. A., Fang, X., Bettles, C. J., & Hutchinson, C. R. (2010). The effect of precipitate state on the creep resistance of Mg–Sn alloys. *Scripta Materialia*, *63*(8), 899–902.

Ghosh, R., & Naryanan, G. (2008). Control of three phase, four wire PWPM rectifier. *IIEE Transactions on Power Electronics*, *24*(6), 1444–1452.

Jiang, J., Tong, L., Xu, Z., Bi, G., Cao, C., Li, Y., Chen, T., Fu, W., & Fang, D. (2023). Improvement in the age-hardening response of Mg–7Sn alloy by compressive stress-assisted aging. *Journal of Materials Research and Technology*, *23*, 2601–2611.

Kimura, R., Hatayama, H., Shinozaki, K., Murashima, I., Asada, J., & Yoshida, M. (2009). Effect of grain refiner and grain size on the susceptibility of Al–Mg die casting alloy to cracking during solidification. *Journal of Materials Processing Technology*, *209*(1), 210–219.

Kondori, B., & Benzerga, A. A. (2014). Effect of stress triaxiality on the flow and fracture of Mg alloy AZ31. *Metallurgical and Materials Transactions A*, *45*(8), 3292–3307.

Koren, Z., Rosenson, H., Gutman, E. M., Unigovski, Y. B., & Eliezer, A. (2002). Development of semisolid casting for AZ91 and AM50 magnesium alloys. *Journal of Light Metals*, *2*(2), 81–87.

Li, G., Zhang, J., Wu, R., Liu, S., Song, B., Jiao, Y., Yang, Q., & Hou, L. (2019). Improving age hardening response and mechanical properties of a new Mg–RE alloy via simple pre-cold rolling. *Journal of Alloys and Compounds*, *777*, 1375–1385.

Luo, J., Mei, Z., Tian, W., & Wang, Z. (2006). Diminishing of work hardening in electro-formed polycrystalline copper with nano-sized and uf-sized twins. *Materials Science and Engineering: A*, *441*(1–2), 282–290.

Mendis, C. L., Bettle, C. J., Gibson, M. A., & Hutchinson, C. R. (2006). An enhanced age hardening response in Mg–Sn based alloys containing Zn. *Materials Science and Engineering: A*, *435–436*, 163–171.

Merson, E., Poluyanov, V., Myagkikh, P., Merson, D., & Vinogradov, A. (2020). Fractographic features of technically pure magnesium, AZ31 and ZK60 alloys subjected to stress corrosion cracking. *Materials Science and Engineering: A*, *772*, 138744.

Nakata, T., & Kamado, S. (2023). Towards tailoring basal texture of rolled Mg alloy sheet by recrystallization for high room-temperature formability: A review. *Journal of Magnesium and Alloys*, *11*(11), 3992–4010.

Nie, J. F. (2003). Effects of precipitate shape and orientation on dispersion strengthening in magnesium alloys. *Scripta Materialia*, *48*(8), 1009–1015.

Peng, P., Yu, D., Guo, X., Zhang, P., Chai, S., Dai, Q., & Lu, J. (2023). Significant improvement in formability and ductility of AZ31 Mg alloy by differential temperature rolling. *Journal of Materials Research and Technology*, *26*, 1293–1305.

Pollock, T. M. (2010). Weight loss with magnesium alloys. *Science*, *328*(5981), 986–987.

Shabani, A., Toroghinejad, M. R., Shafyei, A., & Logé, R. E. (2019). Evaluation of the mechanical properties of the heat treated FeCrCuMnNi high entropy alloy. *Materials Chemistry and Physics*, *221*, 68–77.

Shi, Q., Wang, C. J., Deng, K. K., Fan, Y. D., Nie, K. B., & Liang, W. (2023). Work hardening and softening behaviours of Mg-Zn-Gd-Ca alloy regulated by bimodal microstructure. *Journal of Alloys and Compounds*, *938*, 168606.

Srinivasan, A., Swaminathan, J., Gunjan, M. K., Pillai, U. T. S., & Pai, B. C. (2010). Effect of intermetallic phases on the creep behavior of AZ91 magnesium alloy. *Materials Science and Engineering: A*, *527*(6), 1395–1403.

Wan, Y. J., Zeng, Y., Zeng, Q., Song, B., Huang, X. F., Qian, X. Y., & Jiang, B. (2021). Simultaneously improved strength and toughness of a Mg–Sn alloy through abundant prismatic lath-shaped precipitates. *Materials Science and Engineering: A*, *811*, 141087.

Wang, H. Y., Nan, X. L., Zhang, N., Wang, C., Wang, J. G., & Jiang, Q. C. (2012). Strong strain hardening ability in an as-cast Mg–3Al–3Sn alloy. *Materials Chemistry and Physics*, *132*(2–3), 248–252.

Wang, M. Y., Xu, Y. J., Jing, T., Peng, G. Y., Fu, Y. N., & Chawla, N. (2012). Growth orientations and morphologies of α-Mg dendrites in Mg–Zn alloys. *Scripta Materialia*, *67*(7–8), 629–632.

Xu, T., Feng, Y., Jin, Z., Song, S., & Wang, D. (2012). Determination of the maximum strain-hardening exponent. *Materials Science and Engineering: A*, *550*, 80–86.

Yamamoto, K., Takahashi, M., Kamikubo, Y., Sugiura, Y., Iwasawa, S., Nakata, T., & Kamado, S. (2020). Effect of Mg content on age-hardening response, tensile properties, and microstructures of a T5-treated thixo-cast hypoeutectic Al–Si alloy. *Materials Science and Engineering: A*, *798*, 140089.

You, S., Huang, Y., Kainer, K. U., & Hort, N. (2017). Recent research and developments on wrought magnesium alloys. *Journal of Magnesium and Alloys*, *5*(3), 239–253.

Zhang, D., Zhang, D., Zhang, Y., Chen, S., Xu, T., & Meng, J. (2021). Analysis of strain hardening behavior in a ductile Mg–Yb based alloy. *Materials Science and Engineering: A*, *819*, 141462.

Zhang, Y., Liu, J. P., Chen, S. Y., Xie, X., Liaw, P. K., Dahmen, K. A., Qiao, J. W., & Wang, Y. L. (2017). Serration and noise behaviours in materials. *Progress in Materials Science*, *90*, 358–360.

Zhu, X., Yang, H., Dong, X., & Ji, S. (2019). The effects of varying Mg and Si levels on the microstructural inhomogeneity and eutectic Mg2Si morphology in die-cast Al–Mg–Si alloys. *Journal of Materials Science*, *54*(7), 5773–5787.